OPEN ACCESS
IOP Publishing | Songshan Lake Materials Laboratory Materials Futures
Mater. Futures 2 (2023) 035301 (8pp) https://doi.org/10.1088/2752-5724/acdd87

Intrinsic vacancy in 2D defective semiconductor In_2S_3 for artificial photonic nociceptor

Peng Wang, Wuhong Xue*, Wenjuan Ci, Ruilong Yang and Xiaohong Xu*

Key Laboratory of Magnetic Molecules and Magnetic Information Materials of Ministry of Education & School of Chemistry and Materials Science of Shanxi Normal University, Taiyuan 030031, People's Republic of China

E-mail: xuewuhong@sxnu.edu.cn and xuxh@sxnu.edu.cn

Received 30 March 2023, revised 27 May 2023
Accepted for publication 5 June 2023
Published 6 July 2023

Abstract

It is crucial to develop an advanced artificially intelligent optoelectronic information system that accurately simulates photonic nociceptors like the activation process of a human visual nociceptive pathway. Visible light reaches the retina for human visual perception, but its excessive exposure can damage nearby tissues. However, there are relatively few reports on visible light–triggered nociceptors. Here, we introduce a two-dimensional natural defective III–VI semiconductor β-In_2S_3 and utilize its broad spectral response, including visible light brought by intrinsic defects, for visible light–triggered artificial photonic nociceptors. The response mode of the device, under visible light excitation, is very similar to that of the human eye. It perfectly reproduces the pain perception characteristics of the human visual system, such as 'threshold,' 'relaxation,' 'no adaptation', and 'sensitization'. Its working principle is attributed to the mechanism of charge trapping associated with the intrinsic vacancies in In_2S_3 nanosheets. This work provides an attractive material system (intrinsic defective semiconductors) for broadband artificial photonic nociceptors.

Supplementary material for this article is available online

Keywords: defective semiconductor, In_2S_3, intrinsic vacancy, artificial photonic nociceptors

1. Introduction

Intelligent and human-like robots are essential trends in the development of robots in the future. In particular, humanoid robots with artificial intelligence algorithm functions could be used not only for personal assistance and care in daily life but also for search and rescue in dangerous tasks [1–5]. The robot's perception system could collect data from the outside world and generate different responses according to changes in the external environment, which is vital for improving the service quality and lifespan of the robot. The nociceptor in the perception system, discovered by Julius and Patapoutian, who were awarded the Nobel Prize in physiology and medicine in 2021, is a key sensory receptor. It can identify potential dangers from extreme conditions, such as external temperature, pressure, strong light, and produce early warning signals to be transmitted to the central nervous system for making protective responses avoid the potential physical damage [6, 7]. When the values of electric pulses, generated

* Authors to whom any correspondence should be addressed.

by the noxious stimuli, exceed a certain threshold level, the nociceptors demonstrate strong and rapid responses [4, 6–8]. They exhibit some unique characteristics, such as 'relaxation', 'no adaptation,' 'allodynia,' and 'hyperalgesia,' which are related to the intensity, duration, and repetition rate of external stimuli.

An artificial photonic nociceptor that can faithfully emulate the characteristics of a retina nociceptor, regarded as a key bionic function to protect human vision, is highly desired for the development of advanced intelligent optoelectronic information systems. Recently, an artificial ultraviolet (UV) nociceptor was constructed based on wide-bandgap metal oxides; for instance, Kumar *et al* [6] demonstrated UV light–triggered nociceptive behavior using a ZnO/ATO/FTO heterostructure based on charge trapping/detrapping and Wei *et al* [9] implemented UV nociceptor using SnO_2 nanoparticles generating carriers under UV light irradiation. In addition to UV light, other wavelengths of light, such as visible light, can still cause damage to tissue upon overexposure [10–13]; therefore, it is extremely important to simulate nociceptor characteristics in a wide wavelength range. Gong *et al* [14] reproduced the pain perception characteristics under visible light irradiation in a simple ITO/CeO_{2-x}/Pt sandwich structure. Xu *et al* [15] reported that the Au/$Ga_2O_3(N_2)$:TiO_2/ITO device responded to a wide range of visible light spectra with high-level similarities to the functionalities of optical nociceptors in the human eye. The above artificial photonic (e.g., UV and visible light) nociceptors are based on oxide materials. Thus, it is crucial to explore new material systems for wide-spectrum artificial visual nociceptors.

Here, a natural defective III–VI semiconductor In_2S_3 was introduced to construct a phototransistor for simulating key characteristics of artificial nociceptors using vacancy-inducing broad spectrum response. First, we prepared high-quality 2D In_2S_3 nanosheets via chemical vapor deposition (CVD) technology. As-grown nanosheets have significant vacancy defects and broad spectral absorption, which are very useful for imitating broadband wavelength light-excited nociceptors. In this draft, we primarily demonstrate a visible light–triggered artificial photon nociceptor. The key characteristics of nociceptors, including threshold, adaptation, relaxation and sensitivity, were well imitated, which are attributed to the charge trapping of the vacancies in the In_2S_3 nanosheets. This work demonstrates that two-dimensional (2D) defective III–VI semiconductor materials have immense potential for smart optical sensor systems.

2. Methods

2.1. Synthesis of 2D In_2S_3 nanosheets

The growth process is described as follows. First, S (2 g) and InI (0.5 g) powders were weighed and placed in the low- and high-temperature zones, respectively, and mica with ultra-smooth surface and absence of dangling bonds was used as substrate and placed downstream about 10–15 cm away from the high-temperature zone. The quartz tube was then cleaned with high-purity argon. Next, the low- and high-temperature zones were heated up to 300 °C at a rate of 10 °C min^{-1} and 660 °C at a rate of 22 °C min^{-1} with 60 sccm Ar, respectively, and then maintained for 10 min for the growth of In_2S_3. Finally, the furnace was cooled to room temperature.

2.2. Characterization

The In_2S_3 nanosheets are characterized by the following means: an optical microscope (CeWei LW300LJT), an atomic force microscope (Bruker Dimension Icon), a confocal Raman spectroscopy (Horiba LabRAM HR Evolution, 532 nm), an x-ray photoelectron spectroscopy (XPS, Thermo K-Alpha+ with Al Kα radiation as x-ray source for radiation), a transmission electron microscope (TEM) (JEM-2100) equipped with an energy-dispersive x-ray device and a micro-area UV–vis–NIR optical absorption spectroscopy (Metatest, MStarterABS).

2.3. Device preparation and measurement

The devices were fabricated after transferring β-In_2S_3 nanosheets onto SiO_2/Si (∼285 nm) substrate. Electrodes patterns were defined by MicroWriter Baby Plus. Then, Cr (∼10 nm)/Au (∼100 nm) electrodes films were deposited using a thermal evaporation system. All photoelectric measurements were characterized at room temperature using a lakeshore probe station in a vacuum chamber (10^{-6} Torr) with a Keithley 4200A-SCS semiconductor parameter analyzer combining commercially available LED lights as light source. The optical power densities were detected by the Fieldmate + PM150X photometer.

3. Results

The process of perception and transmission of light by the optic nerve is as follows: light triggers the photoreceptor cells in the retina to generate an electrical response to light. The generated signals pass through the visual pathways and eventually project onto the cerebral cortex to form visual information [16, 17]. In the process of visual signal transmission, there are several electrical and chemical transmissions within or between retinal neurons to process the visual information in the retina [18]. Figure 1(a) shows a typical visual nociceptor nervous system under visible light stimulation. A schematic diagram of the working principle of a visual nociceptor is shown in figure 1(b). Once the optical signal reaches the nociceptor, it will operate in two different ways depending on the signal strength. When the input signal is lower than the threshold value, the device will not generate photoelectric signals, but when the input signal is higher than the threshold value, the device will respond quickly [6, 14, 19]. Figures 1(c)–(e) depict In_2S_3 defective semiconductor-based two terminal planar devices for mimicking a visual nociceptor. The threshold value is determined by vacancy defects in In_2S_3 as capture sites to capture photogenerated carriers, which is different from In_2S_3 polycrystalline thin film [20]. The 'threshold' characteristics of the device are reasonably explained in figures 1(c)–(e). If the optical stimulus is

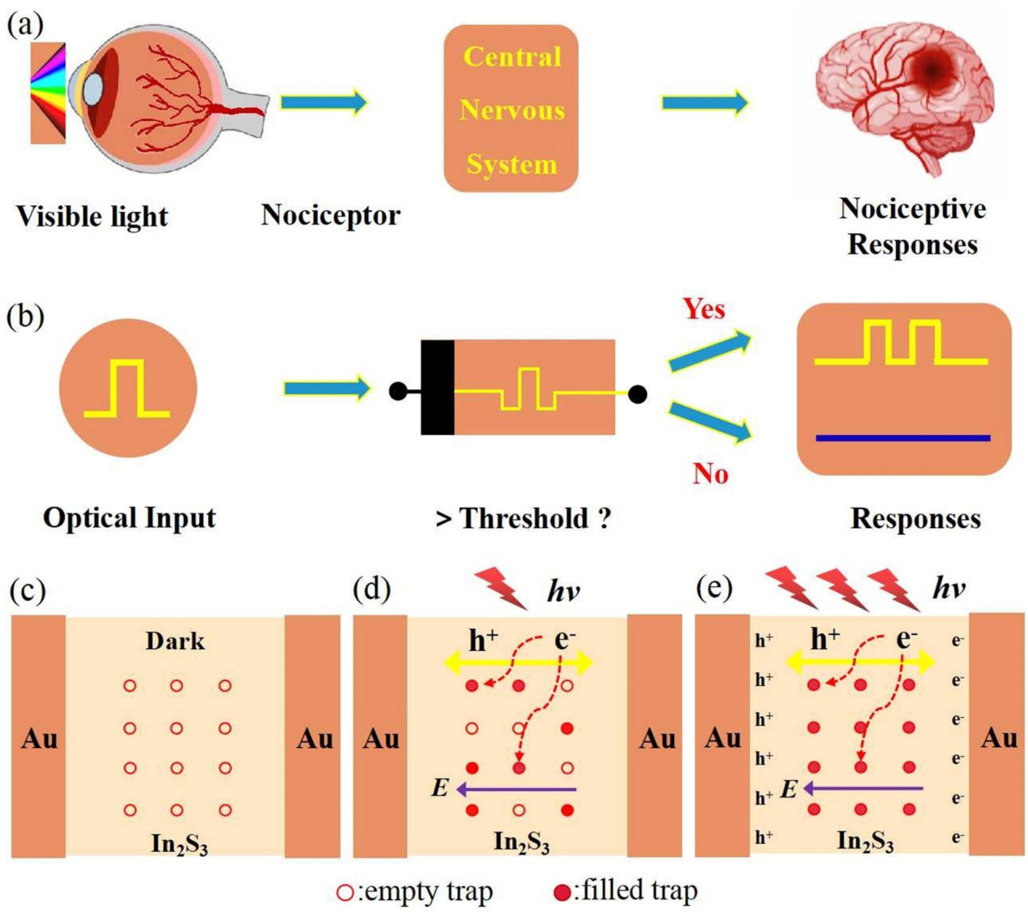

Figure 1. The photonic nociceptive system in the human eyes and the principles of the artificial photonic nociceptor. (a) Neurotransmission processes after the human eyes being injured. (b) Threshold-intensity-dependent photoresponse of the In_2S_3 phototransistor. The current response mechanism diagrams of the designed intrinsic defective semiconductor In_2S_3-based artificial photonic nociceptor in the (c) initial, (d) subthreshold, and (e) overthreshold states.

below the threshold, the photogenerated-free electrons will be trapped by the empty trap sites, resulting in negligible photocurrents in figure 1(d). In contrast, when the optical stimulus is higher than the threshold, abundant photogenerated carriers rapidly fill the trapping sites, and the remaining electrons can be excited into the conduction band and then migrate to the Au electrode by a constant electric field, thereby generating a significant photocurrent in the external circuit (figure 1(e)).

High-quality In_2S_3 nanosheets were first synthesized on the mica substrates by CVD technique (see more in the 'Methods'). Figure 2(a) depicts an optical micrograph as grown triangular In_2S_3 nanosheets indicating a uniform growth. The typical Raman spectrum peaks at 246 cm^{-1}, 266 cm^{-1}, 306 cm^{-1}, 328 cm^{-1}, and 366 cm^{-1} were observed in figure 2(b). These Raman characteristic peaks are very consistent with cubic β-In_2S_3 [21–23]. Furthermore, XPS was also applied to check the elemental composition and bonding state of the nanosheet. The chemical states of $S2p_{1/2}$ and $S2p_{3/2}$ can be identified from the peaks at binding energies of 162.7 and 161.7 eV (figure S1(a)), and the other two fitted peaks at 444.9 and 452.5 eV correspond to the $3d_{1/2}$ and $3d_{3/2}$ states of In, respectively (figure S1(b)) [23–25]. From the XPS full spectrum, the S/In stoichiometric atomic ratio is $\sim$1.5 (figure S1(c)). Furthermore, the energy dispersive x-ray spectroscopy (EDS) of the sample shows clear peaks of In–K_α and S–K_α (figure S2(b)), and element mapping analysis demonstrates the uniform distribution of In and S (figures S3 (b) and (c)). The above results further identify that the synthesized nanosheets are In_2S_3. To further check the crystalline information of the nanosheet, the TEM analysis was performed to visualize the structure of the samples transferred to a copper grid by the poly(methyl methacrylate)-mediated technology [26]. Low-magnification TEM images of the In_2S_3 nanosheet show consistent color contrast, indicating that the edge contour of the nanosheet is regular and the thickness is relatively uniform (figure S3(a)). Figure 2(c) shows high-resolution transmission electron microscopy (HRTEM) image of the nanosheet with clear lattice fringes of (220) crystal planes with a d-spacing of $\sim$0.38 nm, confirming that the as-prepared samples have a preferential orientation along cubic β-In_2S_3 [220] direction on mica substrates [23, 25]. The selected area electron diffraction pattern displays a hexagonal diffraction pattern with equal interplanar distance (figure S2 (a)), further indicating the single-crystalline cubic phase structure (β-In_2S_3). Moreover, the evident vacancy defects marked by white circles were observed (figures 2(c) and S4), which is consistent with the reported contents [23]. In addition, the photoluminescence (PL) and UV to near-infrared (UV-NIR) absorption spectra of

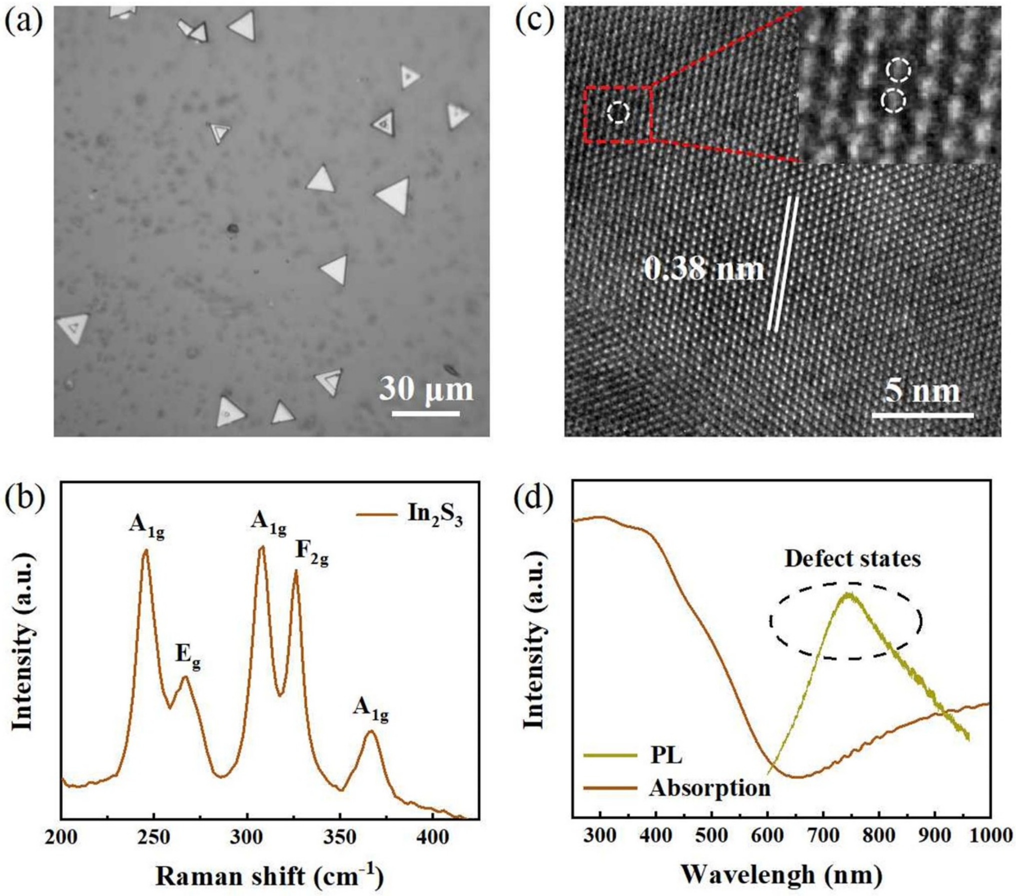

Figure 2. The structure and spectrum characteristics of In_2S_3 nanosheets. (a) Optical image. (b) Typical Raman spectrum of In_2S_3 nanosheet. (c) HRTEM image of sample with a lattice spacing of ∼0.38 nm. Inset: an enlarged view of the red box. (d) The absorption and PL spectra of In_2S_3 nanosheets. The samples have obvious vacancy defects.

β-In_2S_3 nanosheet were characterized to detect defects and light absorption range. An obvious broad spectrum absorption in the range of 250–1000 nm was observed (figure 2(d), brown curve), which is a prerequisite for a wide spectrum visual sensor (e.g., visual nociceptor). A long extended tail (up to 650 nm) in the absorption spectrum can be attributed to the vacancy defect states [27]. Simultaneously, the presence of defect states was also confirmed by PL measurements. The PL spectrum exhibits a strong peak near 745 nm (figure 2(d), green curve), which is attributed to the E_d transition caused by the recombination of inherent sulfur and indium vacancies ($V_S \rightarrow V_{In}$) in the β-In_2S_3 bandgap, not the bandgap emission [23, 28, 29]. However, we cannot track any bandgap (E_g) signal at room temperature, which may be due to the quenching effect of defect transitions (E_d) below the bandgap [23, 30]. In addition, the broad peak observed in the range of 600–900 nm is attributed to the trap states in In_2S_3 [31–33]. These results reveal that In_2S_3 has intrinsic vacancy defects at lattice sites, not an uncontrollable defect introduced during crystal growth [34, 35]. These intrinsic vacancy defects in the crystal structure will exert a stable and significant impact on the electronic structure and optical performance, thereby affecting the electrical performance and photoelectric detection [36, 37].

Due to the presence of trapped states, it is expected that the photoelectric characteristics of the device can be modulated by the photogenerated carriers filling the trapped states, which is very beneficial for mimicking the characteristics of the visual nociceptor. As a result, a phototransistor was prepared on ∼31.7 nm thick In_2S_3 nanosheet transferred onto SiO_2(285 nm)/Si substrate, and two parallel Cr (10 nm)/Au (100 nm) electrodes were deposited as source and drain with a channel distance of ∼8 μm (figure S5). First, the semiconductor properties of In_2S_3 were measured, and the transfer curves indicate that In_2S_3 is an n-type semiconductor material in figure S6. The photocurrent amplitude of the device is gradually increased by red light (671 nm) irradiation of the same intensity and duration at a reading voltage of 0.5 V (figures 3(a) and (b)). It is worth noting that both photocurrent and dark current gradually increase, indicating that the photogenerated carriers gradually fill the trapped states. When the number of light pulses continues to increase, the photocurrent reaches saturation. These features are very beneficial and useful for simulating nociceptive behaviors. The three key features, namely, 'threshold,' 'no adaptation' and 'relaxation' were first experimentally demonstrated through light pulse measurements of the defective In_2S_3 phototransistor. Figure 3(c) displays the pain-perceptual 'threshold'

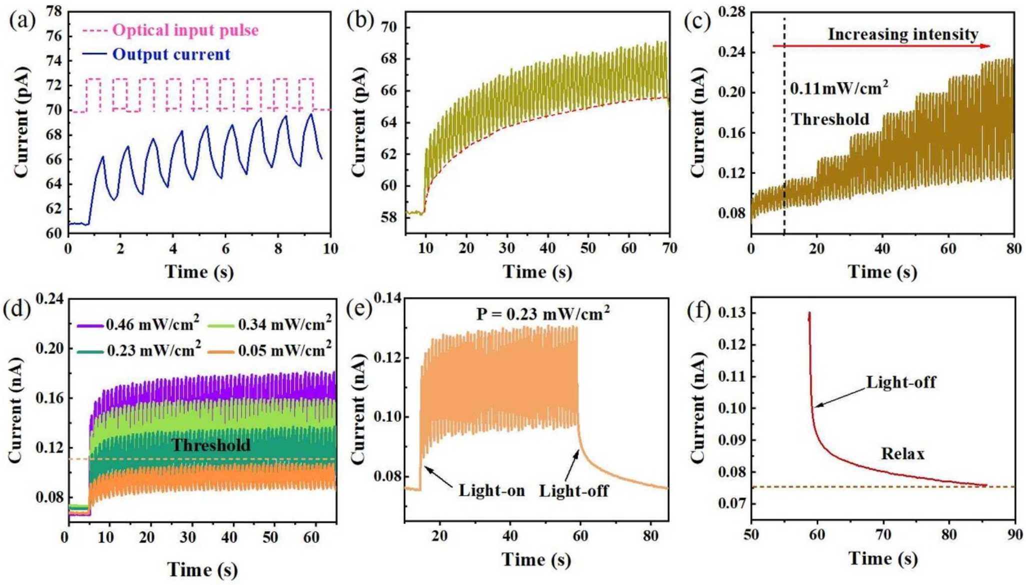

Figure 3. Basic photocurrent characteristics and photonic nociceptive behaviors of the In_2S_3 phototransistor. (a) The photoresponse of the device under nine optical pulses at wavelength of 671 nm. (b) The photocurrent increases with increasing light pulse numbers until it reaches saturation. (c) Threshold characteristic of the device with gradually increasing the light intensity. (d) No adaptation characteristic of devices under different light intensities illumination. (e) Typical photocurrent evolution process of the device under light-on and light-off states. The applied light intensity is $\sim$0.23 mW cm^{-2} and the pulse width is $\sim$0.5 s. (f) The enlarged view of the current relaxation in (e) with decay process of $\sim$25 s.

behavior under the red-light pulse irradiation. When the light intensity was gradually increased from 0.05 to 0.92 mW cm^{-2} with a width of 0.5 s, the device was not turned on until the light intensity reached 0.11 mW cm^{-2} (left side of the black dotted line). The increase in intensity resulted in a larger output of photocurrent, which is consistent with an increase in response intensity corresponding to a higher intensity of noxious stimulus in a biological nociceptor. The 'threshold' characteristics of green and blue light excitation were also well simulated, wherein the threshold value under green light is $\sim$0.08 mW cm^{-2} (figure S7(a)), and the threshold value under blue light is $\sim$0.05 mW cm^{-2} (figure S7(b)). The above results indicate that In_2S_3 device can successfully simulate the 'threshold' characteristic of biological nociceptors in the visible light range. Next, take red light excitation as an example to simulate the characteristics of the 'no adaptation' and 'relaxation.' The light pulses of different intensities (0.05, 0.23, 0.34 and 0.46 mW cm^{-2}) are applied to the device, and the photocurrent gradually reaches saturation; then, it would not change even when additional pulses are applied, indicating a simulation of the characteristics of the 'no adaptation' (figure 3(d)). The saturation of the photocurrent may be attributed to the balance between the trap filling rate of the photogenerated carriers and the spontaneous trap emptying rate [4, 5]. A smooth increase in conductance could arise from the photogenerated carriers gradually filling the trap states [6]. A larger light intensity would fill more trap states until balance is reached, thus promoting conductivity and increasing the saturation current (figure 3(d)). The 'relaxation' is another important characteristic of nociceptors. It means that when the stimulus is removed, the nociceptors begin to relax and eventually return to their original state [6, 38]. It is easy for humans to understand the stronger the response and the longer the relaxation time based on the stronger the injury stimulus and the longer the pain lasts. This relaxation behavior is emulated in the In_2S_3 device. Figure 3(e) shows that applying a continuous light pulse with an intensity of 0.23 mW cm^{-2}, the typical photocurrent evolution process was recorded at a reading voltage of 0.5 V. When the illumination is removed, an obvious current decay process of $\sim$25 s occurred (figure 3(f)). This response is similar to the 'relaxation' behavior of the nociceptor.

Furthermore, the main feature of nociceptor is to show the sensitization including an 'allodynia' and 'hyperalgesia' behaviors for protecting an injured area from further damage by enhancing the pain [39], as presented schematically in figure 4(a). After injury, the nociceptor must show the enhanced response at a reduced threshold [4, 9, 18]. These features are called 'hyperalgesia' and 'allodynia,' as presented by horizontal and vertical arrows in figure 4(a), respectively. Herein, higher intensity light (1.8 mW cm^{-2}) induced the injured condition. The photocurrent of the device under injured and normal conditions is presented by red and blue lines in figure 4(d), respectively. The 'undamaged' nociceptor had a lower photocurrent response, but after strong light illumination, the photocurrent of the 'injured' nociceptor changed significantly, and even at the same light intensity, the injured nociceptor could cause the damaged responses through the amplified photocurrent values (figures 4(b), (c) and S8(a)–(e)). This is attributed to the fact that photogenerated carriers under strong light illumination would quickly fill up the trap states and the remaining carriers could move under applying an external electric field. When the light is excited again,

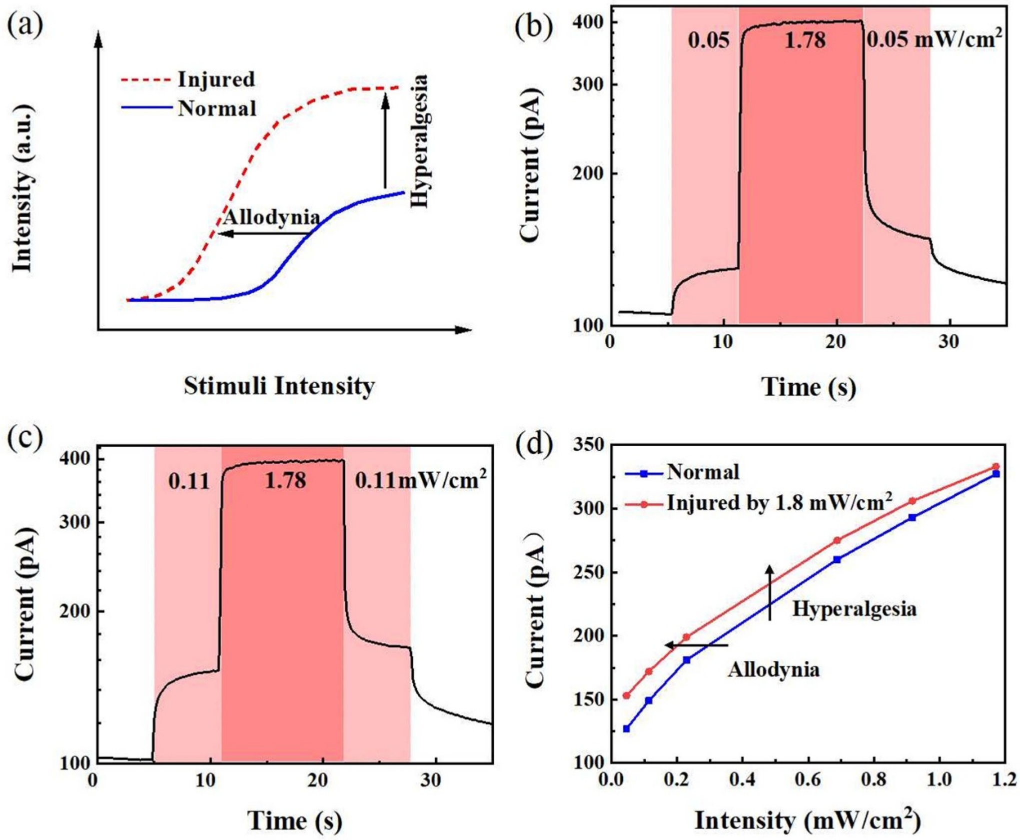

Figure 4. Photonic allodynia and hyperalgesia characteristics of the In_2S_3 device. (a) Schematic of the allodynia and hyperalgesia characteristics with increasing stimuli intensity in normal (no injured) and injured conditions. (b)–(c) The changes in photocurrent after and before strong light stimulation. (d) The photocurrent of the device before and after strong light (1.8 mW cm^{-2}) stimulation showing allodynia and hyperalgesia characteristics.

photogenerated carriers do not need to fill defect states and move in a direct direction to form a current under the action of an electric field, resulting in fast damage responses to reduce the threshold value and to increase the photocurrent values [6, 14]. The above simulation of key visual nociceptor characteristics demonstrates that the intrinsic 2D defective semiconductor In_2S_3-based phototransistor can be well used as an artificial photonic nociceptor.

4. Conclusion

In summary, we propose using the intrinsic 2D defective semiconductor In_2S_3-based phototransistor to simulate broadband spectral-excited visual nociceptor characteristics by the dynamic trapping/detrapping of charges in the vacancy trap states of In_2S_3 nanosheets. Taking visible light (long wavelength red light) as an example, all the key functions of nociceptor have been emulated successfully in a single device, including ‘threshold,’ ‘relaxation,’ ‘no adaptation,’ and ‘sensitization.’ This artificial photonic nociceptor is expected to have good application prospects in a wide spectrum of intelligent optoelectronic systems, such as visual medicine, artificial eyes, and environmental alarms.

5. Future perspectives

Visual sensing, as an important perception of human beings interacting with their environments, is responsible for 80% of the detection information of external stimuli. At present, there is growing interest worldwide in developing artificial devices with the abilities of biological vision. To develop intelligent photoelectric systems that work like human vision systems, it is crucial to develop highly sensitive photoelectric sensors with diverse synaptic functions in a wide spectrum range. In this regard, the development of new materials and working mechanisms for constructing high-performance artificial photoelectric devices are being pursued. The 2D intrinsic defect semiconductor In_2S_3-based artificial photoelectric device has great potential in the future intelligent photoelectric systems. Herein, the device has demonstrated the key characteristics of visual nociceptors under visible light stimulation. Combining its non-volatile photocurrents, it is very promising to realize an all-in-one neuristor in silicon based on 2D intrinsic defect semiconductor materials. In addition, preparing large area 2D intrinsic defect semiconductors, constructing large array devices, and realizing hardware emulation are also very necessary in the future.

Acknowledgments

This work was supported by the National Key Research and Development Program of China (2022YFB3505301), the National Natural Science Foundation of China (12174237, 12241403 and 52002232). Peng Wang completed the preparation and characterization of the device. The manuscript was written by Peng Wang, Wuhong Xue, and Xiaohong Xu. All the authors discussed the results and commented on the manuscript.

Conflict of interest

The authors declare no conflict of interest.

ORCID iDs

Peng Wang https://orcid.org/0009-0002-0397-3484
Wuhong Xue https://orcid.org/0000-0003-2543-8626
Xiaohong Xu https://orcid.org/0000-0001-7588-4793

References

[1] Basbaum A I, Bautista D M, Scherrer G and Julius D 2009 Cellular and molecular mechanisms of pain *Cell* **139** 267–84
[2] Dubin A E and Patapoutian A 2010 Nociceptors: the sensors of the pain pathway *J. Clin. Invest.* **120** 3760–72
[3] Julius D and Basbaum A I 2001 Molecular mechanisms of nociception *Nature* **413** 203–10
[4] Yoon J H, Wang Z, Kim K M, Wu H, Ravichandran V, Xia Q, Hwang C S and Yang J J 2018 An artificial nociceptor based on a diffusive memristor *Nat. Commun.* **9** 417
[5] Xue W, Gao C, Zhang Z, Han T, Hou N, Yin W, Shi L, Wang X, Liu G and Xu X 2022 Native drift and Mott nanochannel in layered V_2O_5 film for synaptic and nociceptive simulation *Sci. China Mater.* **66** 764–71
[6] Kumar M, Kim H S and Kim J 2019 A highly transparent artificial photonic nociceptor *Adv. Mater.* **31** 1900021
[7] Zhou L, Zhang S R, Yang J Q, Mao J Y, Ren Y, Shan H, Xu Z, Zhou Y and Han S T 2020 A UV damage-sensing nociceptive device for bionic applications *Nanoscale* **12** 1484–94
[8] Feng G D *et al* 2020 A Sub-10 nm vertical organic/inorganic hybrid transistor for pain-perceptual and sensitization-regulated nociceptor emulation *Adv. Mater.* **32** e1906171
[9] Wei H H, Ni Y, Sun L, Yu H, Gong J D, Du Y, Ma M, Han H and Xu W 2021 Flexible electro-optical neuromorphic transistors with tunable synaptic plasticity and nociceptive behavior *Nano Energy* **81** 105648
[10] Sliney D H 2002 How light reaches the eye and its components *Int. J. Toxicol.* **21** 501–9
[11] Sliney D H 2001 Photoprotection of the eye—UV radiation and sunglasses *J. Photochem. Photobiol.* B **64** 166–75
[12] Rozanowska M and Sarna T 2005 Light-induced damage to the retina: role of rhodopsin chromophore revisited *Photochem. Photobiol.* **81** 1305–30
[13] Okamoto K, Tashiro A, Chang Z and Bereiter D A 2010 Bright light activates a trigeminal nociceptive pathway *Pain* **149** 235–42
[14] Gong G D, Gao S, Xie Z L, Ye X Y, Lu Y, Yang H L, Zhu X J and Li R W 2021 A visible light-triggered artificial photonic nociceptor with adaptive tunability of threshold *Nanoscale* **13** 1029–37
[15] Xu H, Karbalaei Akbari M, Verpoort F and Zhuiykov S 2020 Nano-engineering and functionalization of hybrid Au-Me_xO_y-TiO_2 (Me = W, Ga) hetero-interfaces for optoelectronic receptors and nociceptors *Nanoscale* **12** 20177–88
[16] Choi C *et al* 2020 Curved neuromorphic image sensor array using a MoS_2-organic heterostructure inspired by the human visual recognition system *Nat. Commun.* **11** 5934
[17] Zhou F C *et al* 2019 Optoelectronic resistive random access memory for neuromorphic vision sensors *Nat. Nanotechnol.* **14** 776–82
[18] Karbalaei Akbari M, Hu J, Verpoort F, Lu H and Zhuiykov S 2020 Nanoscale all-oxide-heterostructured bio-inspired optoresponsive nociceptor *Nano-Micro Lett.* **12** 83
[19] Xiao M, Shen D, Futscher M H, Ehrler B, Musselman K P, Duley W W and Zhou Y N 2019 Threshold switching in single metal-oxide nanobelt devices emulating an artificial nociceptor *Adv. Electron. Mater.* **6** 1900595
[20] Zhao Y *et al* 2021 An artificial optoelectronic nociceptor based on In_2S_3 memristor *J. Appl. Phys.* **55** 125401
[21] Kambas K, Spyridelis J and Balkanski M J P S S 2010 Far infrared and Raman optical study of α- and β-In_2S_3 compounds *Phys. Status Solidi* **105** 291–6
[22] Lu J *et al* 2018 Graphene/In_2S_3 van der Waals heterostructure for ultrasensitive photodetection *ACS Photonics* **5** 4912–9
[23] Huang W, Gan L, Yang H, Zhou N, Wang R, Wu W, Li H, Ma Y, Zeng H and Zhai T 2017 Controlled synthesis of ultrathin 2D β-In_2S_3 with broadband photoresponse by chemical vapor deposition *Adv. Funct. Mater.* **27** 1702448
[24] Xiong X, Zhang Q, Gan L, Zhou X, Xing X, Li H Q and Zhai T Y 2016 Geometry dependent photoconductivity of In_2S_3 kinks synthesized by kinetically controlled thermal deposition *Nano Res.* **9** 3848–57
[25] Zhao Y *et al* 2019 Thickness-dependent optical properties and in-plane anisotropic Raman response of the 2D β-In_2S_3 *Adv. Opt. Mater.* **7** 1901085
[26] Lin M *et al* 2013 Controlled growth of atomically thin In_2Se_3 flakes by van der Waals epitaxy *J. Am. Chem. Soc.* **135** 13274–7
[27] Hu C, Wang Q, Bai S, Xu M, He D, Lyu D and Qi J 2017 The effect of oxygen vacancy on switching mechanism of ZnO resistive switching memory *Appl. Phys. Lett.* **110** 073501
[28] Ho C-H 2010 Growth and characterization of near-band-edge transitions in β-In_2S_3 single crystals *J. Cryst. Growth* **312** 2718–23
[29] Ghorbani E and Albe K 2018 Intrinsic point defects in β-In_2S_3 studied by means of hybrid density-functional theory *J. Appl. Phys.* **123** 103103
[30] Zhou N, Gan L, Yang R, Wang F, Li L, Chen Y C, Li D and Zhai T 2019 Nonlayered two-dimensional defective semiconductor γ-Ga_2S_3 toward broadband photodetection *ACS Nano* **13** 6297–307
[31] Singh A, Senapati K, Satpati B, Kumar M and Sahoo P K 2015 Nanoscale interface engineering in ZnO twin nanorods for proposed phonon tunnel devices *Phys. Chem. Chem. Phys.* **17** 4277–82
[32] Kumar M, Basu T and Som T 2015 Ultra-violet absorption induced modifications in bulk and nanoscale electrical transport properties of Al-doped ZnO thin films *J. Appl. Phys.* **118** 055102
[33] Ghosh A, Guha P, Thapa R, Selvaraj S, Kumar M, Rakshit B, Dash T, Bar R, Ray S K and Satyam P V 2016 Tuning the work function of randomly oriented ZnO nanostructures by capping with faceted Au nanostructure and oxygen defects: enhanced field emission experiments and DFT studies *Nanotechnology* **27** 125701

[34] Marsillac S, Mangale N S, Gade V and Khare S V 2011 Structural and electronic properties of β-In_2X_3 (X = O, S, Se, Te) using *ab initio* calculations *Thin Solid Films* **519** 5679–83

[35] Yuan X Z, Jiang L B, Liang J, Pan Y, Zhang J, Wang H, Leng L J, Wu Z, Guan R and Zeng G M 2019 *In-situ* synthesis of 3D microsphere-like $In_2S_3/InVO_4$ heterojunction with efficient photocatalytic activity for tetracycline degradation under visible light irradiation *Chem. Eng. J.* **356** 371–81

[36] Gopinath G R, Miles R W and Reddy K T R 2013 Influence of bath temperature on the properties of In_2S_3 films grown by chemical bath deposition *Energy Proc.* **34** 399–406

[37] Warrier A R, Bingi J and Vijayan C 2015 Plasmon-assisted enhancement and tuning of optical properties in β-In_2S_3 quantum dots *Plasmonics* **11** 953–61

[38] Kim Y *et al* 2018 Nociceptive memristor *Adv. Mater.* **30** 1704320

[39] Gold M S and Gebhart G F 2010 Nociceptor sensitization in pain pathogenesis *Nat. Med.* **16** 1248–57